Research in Astron. Astrophys. Vol.0 (20xx) No.0, 000–000
http://www.raa-journal.org *http://www.iop.org/journals/raa*
(LaTeX: ms2025-0617.tex; printed on May 19, 2026; 2:01)

***R**esearch in*
***A**stronomy and*
***A**strophysics*

Impact of Satellite Constellations on Observations with the 80-cm Telescope and the Mini-SiTian at the Xinglong Observatory, NAOC

Jing Ren[1,2], Zhou Fan[1,2,6], Hong-rui Gu[1,2], Qi-qian Zhang[1,2], Yun-fei Xu[1,2,3], Jun-ju Du[4], Xiao-han Chen[1,5], Lin-ying Mi[1,2,3] and Hong Wu[1,2]

[1] National Astronomical Observatories, Chinese Academy of Sciences, Beijing 100101, People's Republic of China; *zfan@nao.cas.cn*
[2] School of Astronomy and Space Science, University of Chinese Academy of Sciences, Beijing 100049, People's Republic of China
[3] National Astronomical Data Center of China, Beijing 100101, People's Republic of China
[4] Shandong Key Laboratory of Space Environment and Exploration Technology, Institute of Space Sciences, School of Space Science and Technology, Shandong University, Shandong, China
[5] School of Physics and Astronomy, China West Normal University, Nanchong 637002, People's Republic of China
[6] Corresponding author: Zhou Fan(zfan@nao.cas.cn)

Received 20xx month day; accepted 20xx month day

Abstract The rapid development of mega-constellations in low Earth orbit (LEO) severely impacts ground-based optical astronomical observations. By combining WorldWide Telescope (WWT) simulations with 2019 and 2023 observational data from the Xinglong Observatory 80-cm telescope and 2023 data from the Mini-SiTian (MST), we find that satellite visibility increases with deployment, particularly during the summer. For the 80-cm telescope, the fraction of images containing satellite trails increased from an average of 0.34% in 2019 to 0.7% in 2023; meanwhile, for the MST in 2023, the fraction rose from 5% in January to 12% by December, peaking at 19% in the summer. Through stratified analysis of solar elevation and local time, we find that observations during twilight and summer are particularly susceptible to satellite trail interference. Photometric analysis reveals that the interference intensity increases for fainter sources and those closer to the trails. Furthermore, a comparative analysis across different seeing conditions shows that the deviation of median standardized residuals (σ) is significantly greater under poor seeing than under good seeing conditions.

Key words: light pollution, telescopes, methods: observational

1 INTRODUCTION

Since the launch of the first artificial satellite in 1957, the region of space near Earth has undergone a radical transformation. A key driver of this recent change is the proliferation of satellite mega-constellations—vast networks of satellites. Their deployment has led to a rapid expansion of the satellite population in LEO, with the number of active satellites more than doubling since early 2019 (Barentine et al. 2023). Currently, mega-constellation satellites constitute an emerging source of astronomical light pollution. In recent years, rapid advancements in space communication technologies and significant

reductions in satellite launch costs have sparked a rapid acceleration in the development of LEO satellite constellations. This development is trending toward massive, large-scale deployments (Muirhead et al. 2025). The Starlink project, leveraging the rapid growth of SpaceX's space industry, exemplifies this trend. SpaceX has received approval from the U.S. Federal Communications Commission (FCC) to operate up to 12,000 satellites. Subsequently, the company filed an application with the FCC for an additional 30,000 Starlink satellites, bringing the total planned constellation size to 42,000 (Halferty et al. 2022). Since the launch of the first batch of 60 Starlink satellites by SpaceX in May 2019, the astronomical community has persistently expressed concerns about the potential adverse impacts these satellites may have on ground-based astronomical observations (McDowell 2020). Other companies, such as OneWeb, Amazon, and Samsung, along with national agencies, are also planning similar LEO satellite constellations. Currently, there are 43 mega-constellation programs still in the development phase(Zhi et al. 2024). According to regulatory filings with the International Telecommunication Union (ITU), approximately 100,000 satellites are projected to be launched into LEO within the next decade (Krantz et al. 2021). Table 1 lists some information for frequently mentioned mega-constellations.

Gallozzi et al. (2020) quantified ground-based astronomical damage; they argued that due to satellite disruption, the loss in the value of public investment in each facility varies directly with the loss of the associated scientific output. Data contaminated by satellite interference frequently require exclusion, thereby eroding the return on investment for both high-cost research facilities and the subsequent mitigation efforts (Kruk et al. 2023). These losses amount to hundreds of millions in public funds annually, potentially totaling tens of billions over the coming decades. If the number of satellites in LEO reaches 100,000, this scenario would inflict incalculable damage not only to ground-based astronomical observations but also to space exploration as a whole (Gallozzi et al. 2020).

Multiple studies—including the Satellite Constellations 1 and 2 (SATCON1 and SATCON2) workshops and the Dark and Quiet Skies for Science and Society workshops—have investigated the impact of satellite constellations on astronomical observations. The SATCON1 report also incorporates extensive observations of Starlink satellites. Collectively, these data confirm that concerns regarding the preservation of the night sky are well-founded: satellites currently in orbit exhibit high apparent brightness. When illuminated by sunlight, many units are visible to the unaided eye, particularly since their brightness levels remain currently subject to no international regulatory limits (Mróz et al. 2022). Several astrophysical research domains are identified by Walker et al. (2020) as critically vulnerable to the effects of large LEO satellite constellations, including observations of rare transients, deep and wide extragalactic imaging, searches for near-Earth objects (NEOs), and deep wide-field near-infrared (NIR) surveys.

McDowell (2020) surveyed the current population of artificial satellites in LEO and modeled the impacts of various satellite constellations on ground-based observatories at different geographic locations. The study noted particularly severe impacts on twilight observations, long-exposure wide-field exposures, high-latitude observatories, and observations during local summer. Mróz et al. (2022) analyzed Zwicky Transient Facility (ZTF) data from November 2019 to September 2021 and reported a strong correlation between the increasing number of SpaceX satellites and the frequency of image contamination. Specifically, twilight observations were most severely impacted, with the fraction of compromised frames increasing from less than 0.5% to 18%. This trend led to the projection that nearly all ZTF twilight exposures will contain satellite trails once the Starlink constellation reaches 10,000 units. Bassa et al. (2022) performed comprehensive simulations to evaluate the impact of satellite constellations on various astronomical instruments, including both imagers and spectrographs. Lawler et al. (2021) developed a satellite reflectance model calibrated with Starlink observations to predict apparent magnitudes and spatial distributions of satellites as a function of geographic coordinates, season, and time. The results indicate that Starlink satellites at an altitude of 550 km remain persistently visible throughout summer nights at mid-to-high latitudes. Tyson et al. (2020) analyzed the effects of satellite constellations on the Vera C. Rubin Observatory's Legacy Survey of Space and Time (LSST), empirically determining that satellites brighter than $V \approx 7$ mag induce nonlinear CCD cross-talk artifacts.

In response to strong advocacy from the astronomical community, SpaceX has developed new designs aimed at reducing satellite reflectivity. These mitigation strategies include the use of experimental

coatings to diminish the albedo and fitting the spacecraft with deployable sunshades. In 2020, SpaceX implemented its initial mitigation attempt with "DarkSat" (Starlink-1130), which featured an experimental black darkening coating (Tregloan-Reed et al. 2020). Tregloan-Reed et al. (2020) and Halferty et al. (2022) reported a reduction in optical brightness, but Horiuchi et al. (2020) reported that it was brighter. In either case, significant solar absorption caused thermal management issues, leading to the abandonment of this strategy. The subsequent iteration involved the deployment of the "VisorSat" design, which was equipped with deployable sunshades. This modification significantly reduced satellite brightness (Mallama et al. 2023b).

In this study, we assess the impact of artificial satellites on observations with the 80-cm telescope and the MST at the Xinglong Observatory by integrating simulation and observational approaches. Using the WWT, we simulate Starlink satellite visibility and quantify the number of illuminated spacecraft as a function of date and time of night. We then analyze observational data from both instruments, employing the probabilistic Hough transform to detect satellite trails and calculating the fraction of images containing satellite trails. Subsequently, we quantify the fraction of sources affected by satellite trails. Furthermore, for trail-contaminated images acquired by the MST, we perform aperture photometry to derive standardized residuals between measured magnitudes and Gaia catalog magnitudes. The sources are then grouped by both their distance from the satellite trail and their magnitude to analyze the degree of impact on sources at different distances and with varying magnitudes.

The paper is structured as follows: in Section 2, we simulate the visibility of Starlink satellites using the WWT to evaluate their impact on observations at the Xinglong Observatory. Section 3 employs the probabilistic Hough transform to detect satellite trails within the 80-cm telescope datasets from 2019 and 2023, as well as MST data from 2023, quantifying the fraction of images containing satellite trails. Section 4 presents a photometric analysis of trail-contaminated MST images to assess the impact on sources at various distances from the trail and across different brightness levels. Section 5 discusses these findings in the context of current research. Finally, Section 6 provides a summary and future outlook.

Table 1: Information of Several LEO Mega-constellations

No.	Constellation	Manufacturer	Altitude (km)	Satellites
1	Starlink Generation 1	SpaceX	335-560	11,926
2	Starlink Generation 2	SpaceX	328-614	30,000
3	Project Kuiper	Amazon	590-630	3,236
4	OneWeb Phase 1	OneWeb/Airbus	1200	1,980
5	OneWeb Phase 2	OneWeb/Airbus	1200	6,372
6	GuoWang GW-A59	CASC	508-1,145	12,992
7	Hanwha System	Hanwha	Unknown	2,000

2 SIMULATION WITH THE WORLDWIDE TELESCOPE

We simulate the visibility of Starlink satellites using the WWT to assess their impact on observations at the Xinglong Observatory. We quantify the number of Starlink satellites visible from this site throughout 2023, including targeted seasonal analyses for summer and winter as a function of date and time.

2.1 WorldWide Telescope

The WWT is an open-source astronomical data visualization platform, originally developed by Microsoft Research and now maintained by the American Astronomical Society (Xu et al. 2020; Rosenfield et al. 2018). The WWT boasts powerful spatiotemporal simulation capabilities, enabling the simulation of celestial events for any specified time and location. Its Sats Tracker module simulates satellite visibility, while the Obs Simulator module loads and visualizes telescope observation plan files, simultaneously simulating the observed sky regions and satellite motion (Cui & Xu 2022).

2.2 Impact of Starlink Satellites on observations at the Xinglong Observatory

Based on the capabilities of the WWT, taking Starlink as a representative constellation, we simulate the impact of Starlink on the observable sky regions of the Xinglong Observatory throughout 2023. The simulation quantifies the number of Starlink satellites visible from the observatory. Furthermore, we simulate the number of visible Starlink satellites as a function of date and time of night for both summer and winter. The Xinglong Observatory of the National Astronomical Observatories, CAS (NAOC), was founded in 1968, and it is located in the south of the main peak of the Yanshan Mountains, in the Xinglong County, Hebei Province, which is $\sim 120\,\mathrm{km}$ northeast of Beijing. Its geographical coordinates are $117°34.5'$ E longitude and $40°23'36''$ N latitude. The average altitude of the Xinglong Observatory is $\sim 960\,\mathrm{m}$. It is one of the primary observing stations of NAOC. As one of the largest optical astronomical observatory sites in the continent of Asia, it harbors nine telescopes with an effective aperture greater than 50 cm (Fan et al. 2016).

We employ the 1st and 15th of each month as designated sampling dates. For each date, we compute time windows during which the solar elevation angle is below $-12°$, spanning from the end of evening nautical twilight to the beginning of morning nautical twilight. This is because satellite visibility depends on the sunlight it reflects and the sky's brightness. Only after the Sun is below a certain elevation angle can these two factors lead to a bright satellite. Therefore, we choose a Sun elevation angle of $-12°$ as the limit (Cui & Xu 2022). We retrieve Starlink satellite orbital data from the Space-Track website. This website publishes Starlink orbital data in Two-Line Element (TLE) format, which is derived from ephemerides provided by SpaceX and is accessible via a dedicated API. Subsequently, the Sats Tracker module divides the simulation period into 5-second time intervals, sequentially computing which satellites appear within the observable sky region of the observatory during each interval. Following the computation of all time slices, the start and end times of each satellite's visible period are determined. Furthermore, since most telescopes have a pointing limit of at least $30°$ above the horizon, detected satellites with a maximum elevation below $30°$ are excluded from the analysis.

Figure 1 shows the number of Starlink satellites in orbit, the number of visible Starlink satellites at the Xinglong Observatory, and their corresponding visibility ratio for each sampling date. The total number of in-orbit Starlink satellites exhibits an overall upward trend with successive launches. As the number of Starlink satellites increases, the number of visible Starlink satellites similarly follows an upward trajectory. As shown in the plot, the fraction of visible satellites in summer is significantly higher than in other months. We then simulate the number of these Starlink satellites that are visible as a function of date and time of night. As a representative case, we simulate the visibility of Starlink satellites during both the summer and winter. The number of visible Starlink satellites in summer and winter is presented in Figure 2, respectively. Notably, the visibility window is significantly protracted during summer. During this period, satellites remain illuminated throughout the night, spanning the entire interval between evening and morning nautical twilights. In contrast, during winter, satellites are primarily visible only during twilight.

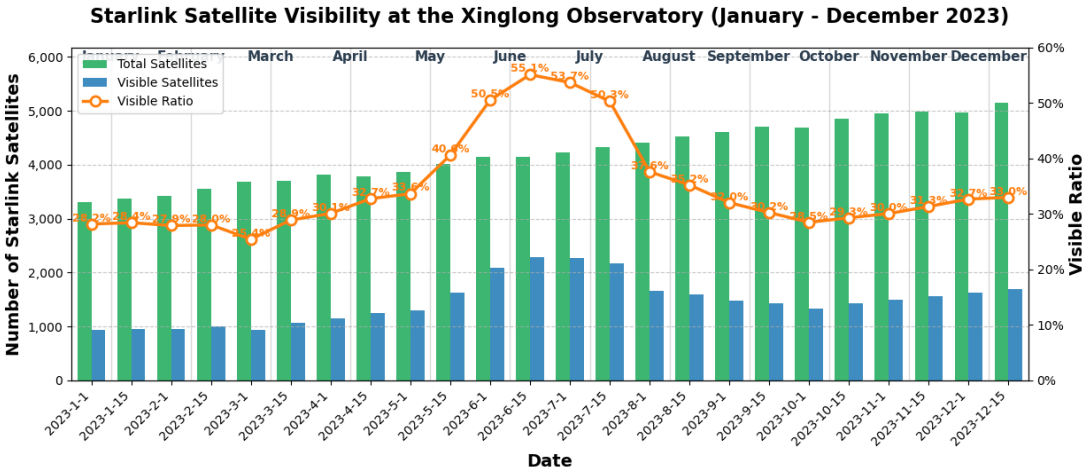

Fig. 1: From January to December 2023, the number of Starlink satellites in orbit and the number of Starlink satellites visible from the Xinglong Observatory. Green bars represent the total number of in-orbit Starlink satellites, blue bars indicate the number of visible Starlink satellites, and the orange line plots the ratio of visible to total satellites.

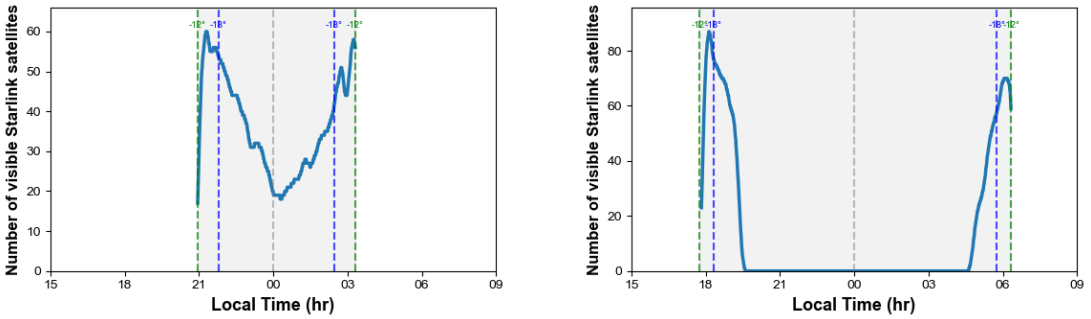

Fig. 2: Starlink satellites visible from the Xinglong Observatory in summer (Jun 15) (left) and winter (Dec 15) (right), versus time of night. Vertical lines indicate the times at which the sun reaches elevations $-12°$ and $-18°$ degrees for the ground observer.

3 DETECTING ARTIFICIAL SATELLITE TRAILS

To assess the impact of artificial satellites on observations with the 80-cm telescope and the MST, we apply the Probabilistic Hough Transform (PHT) to detect satellite trails in the 80-cm telescope (2019, 2023) and MST (2023) datasets. We subsequently calculate the fraction of trail-contaminated images on a monthly basis. To account for the non-uniform observation time across different months, we further determine the hourly trail-contaminated fraction for both facilities. Furthermore, we analyze the monthly fraction of images containing satellite trails categorized by solar elevation angle intervals, specifically focusing on the ranges from $-20°$ to $-12°$ and$-35°$ to $-25°$.

Although individual exposure times vary (predominantly ranging from 100 s to 300 s), we have verified that the distribution of these durations is statistically consistent across different months. Since a satellite typically crosses the field of view in much less than 100 s, any exposure within this range is equally capable of capturing a trail. Thus, the "fraction of contaminated images" serves as a robust proxy for the probability of interference per observing session.

3.1 Data

We utilize a total of 96,450 images captured by the 80-cm telescope at the Xinglong Observatory in 2019 and 2023, along with 27,205 images obtained by the MST in 2023. We detect satellite trails within these datasets using the PHT. Due to telescope maintenance in July and August, no observations acquired during these two months. The 80-cm telescope, known as the Tsinghua-NAOC Telescope (TNT), is a collaborative facility between Tsinghua University and NAOC. This instrument features an 80-cm aperture with a focal length of 8 m in a classical Cassegrain configuration, mounted on an equatorial platform. Its field of view spans $11.4' \times 11.1'$. All these parameters of instruments are summarized in Table 2. The MST project is a pathfinder of SiTian (Liu et al. 2021; Huang et al. 2025). The MST is composed of three 30 cm catadioptric Schmidt telescopes: MST-001 (MST1), MST-002 (MST2) and MST-003 (MST3). One filter for each telescope, i, g and r band for MST1, MST2 and MST3, respectively, a wide $2.29^\circ \times 1.53^\circ$ field of view, and a 9K×6K scientific CMOS detector (He et al. 2025; Zhang et al. 2025). All these parameters of instruments are summarized in Table 3.

Table 2: Summary of the 80-cm Telescope

Parameter Category	Specification
Telescope Parameters	
Primary Mirror diameter	$80\,\mathrm{cm}$
Focal Ratio	f/3
Corrected Focal Ratio	f/10
Focal Plane Scale	$25.8\,''\,\mathrm{mm}^{-1}$
Optical System	Classical Cassegrain
Mount Type	Equatorial Mount
Field of View	$11.4' \times 11.1'$
Camera Parameters	
Model	PI VersArray 1300B LN Back-Illuminated Scientific CCD
Pixel Array	$1,340 \times 1,300$ pixels
Pixel Size	$20\,\mu\mathrm{m}$
Pixel Scale	$0.52\,''\,\mathrm{pix}^{-1}$
Operating Temperature	$-110\,^\circ\mathrm{C}$

Table 3: Summary of the MST Telescope Array

Parameter Category	Specification
Telescope Parameters	
Primary Mirror diameter	$30\,\mathrm{cm}$
Number of telescopes	3
Focal Ratio	f/3
Optical System	Catadioptric Schmidt
Mount Type	Fork-type equatorial
Field of View	$5^\circ \times 5^\circ$
Camera Parameters	
Model	ZWO ASI6200MM Pro CMOS
Pixel Array	9,576 × 6,388 pixels
Pixel Size	$3.76\,\mu\mathrm{m}$
Pixel Scale	$0.862\,''\,\mathrm{pix}^{-1}$
Camera FOV	$2.29^\circ \times 1.53^\circ$
Operating Temperature	Cooling $30\,^\circ\mathrm{C}$ below ambient

3.2 Method

This study utilizes the PHT to detect satellite trails. The Hough line detection algorithm transforms the problem of line detection in image space into peak detection within a parameter space. This approach enables the robust identification of linear features, such as satellite trails, by isolating these local maxima. The parameter space is defined by a polar coordinate system, where any line in the image is represented as a point governed by the equation $r = x\cos\theta + y\sin\theta$, where r is the perpendicular distance from the origin to the line, and θ is the angle of the normal with the horizontal axis (Stoppa et al. 2024). Each point (r, θ) in the parameter space maps to a unique line in the image space. Conversely, a single point in the image space generates a sinusoidal curve in the parameter space. For every candidate pixel associated with a satellite trail, the algorithm identifies all potential lines passing through that pixel, each defined by a distinct (r, θ) pair. The intersection points of these curves, derived from distinct pixels, signify a collective agreement on the presence of a straight line in the original image.

The PHT serves as a computationally efficient variant of the standard Hough Transform, detecting linear features by processing random subsets of image points. We rigorously optimized the algorithm parameters as follows:

- *Distance resolution* : 3 pixels (balancing computational speed and spatial precision)
- *Angular resolution*: 1° (providing full 180° coverage)
- *Min line length* : 1000 pixels (aligned with typical satellite trail characteristics)
- *Max gap* : 300 pixels (robust to occlusion effects)
- *Accumulator threshold*: A Critical value separating *bona fide* trails from stochastic noise

This configuration effectively accounts for the specific geometric profiles of LEO satellite streaks. Figure 3 displays images containing satellite trails detected via the PHT from the 80-cm telescope and MST2, respectively.

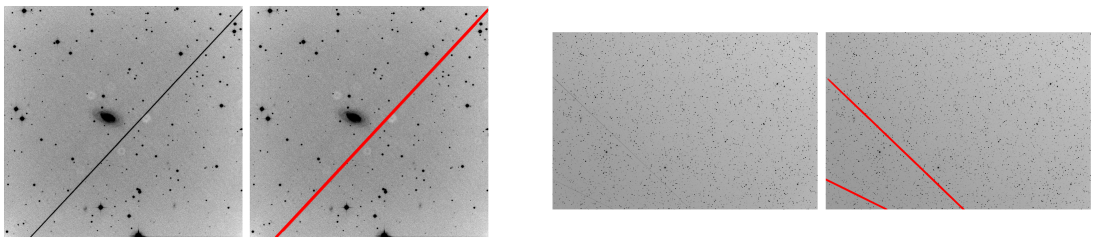

Fig. 3: Original image with satellite trails detected by the PHT and marked by red lines, the 80-cm telescope (left) and the MST2 (right).

3.3 Results

Figure 4 shows the fraction of images containing satellite trails acquired by the 80-cm telescope in 2019 and 2023, while Figure 5 shows this fraction for MST2 observations in 2023. An overall upward trend in image contamination is evident, correlating with expanded satellite constellations. For the 80-cm telescope, the contamination fraction rises from an average of 0.34% in 2019 to 0.7% in 2023. Due to its wider field of view (FoV), the MST2 exhibits a markedly higher fraction of images with satellite trails than the 80-cm telescope. Specifically, the fraction of images containing satellite trails grows from 5% in January 2023 to 12% in December 2023, reaching a peak of 19% in summer.

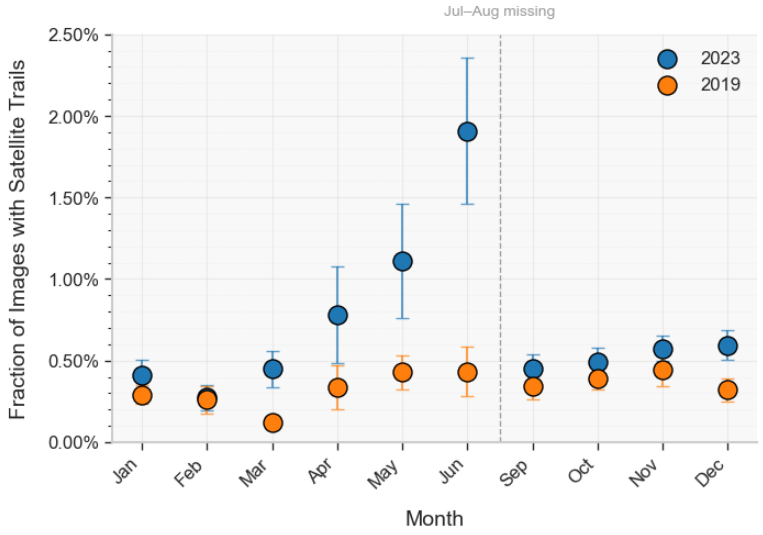

Fig. 4: Fraction of images with satellite trails (80-cm telescope, 2019 vs. 2023): orange dots for 2019, blue dots for 2023.

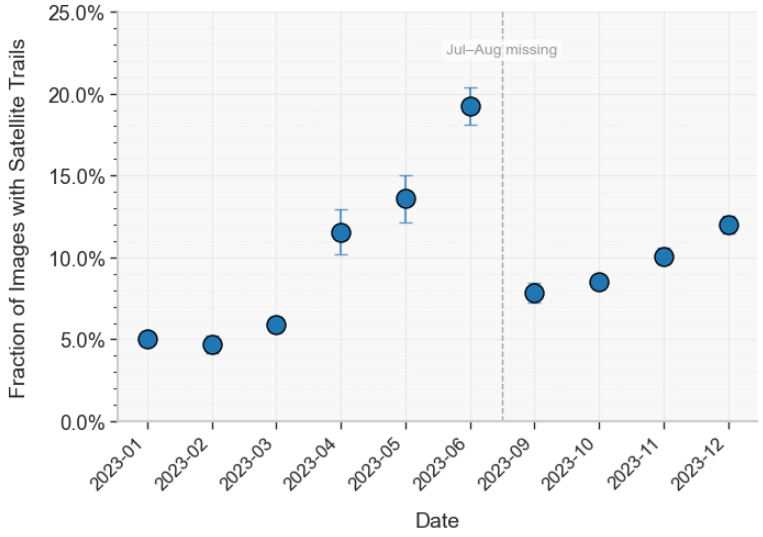

Fig. 5: Fraction of images with satellite trails acquired by MST2 in 2023.

To account for the non-uniform observation time across different months, Figure 6 and Figure 7 show the monthly distribution of the hourly trail-contaminated fraction for the 80-cm telescope and MST2 throughout 2023, respectively. Furthermore, Figure 8 and Figure 9 illustrate the monthly fraction of images containing satellite trails categorized by solar elevation angle intervals, specifically for the ranges from -20° to -12° and-35° to -25°, for both facilities. As illustrated, with the increasing number of satellite deployments, the fraction of trail-contaminated images exhibits an overall upward trend. The impact is particularly severe during twilight; for the wide-field MST2, the affected fraction rose from less than 20% in January to approximately 35% by December 2023. We note that certain short-term fluctuations, such as the increase between March and April, are associated with larger statistical

uncertainties due to smaller sample sizes in specific months (e.g., $N_{\mathrm{Apr}} = 606$ vs. $N_{\mathrm{Mar}} = 2491$), as reflected by the provided error bars.

Regarding deep-night observations, the contamination fraction during the summer is notably higher than in winter. This trend is a direct physical consequence of the LEO orbital geometry during the summer solstice. At the observatory's latitude, the sun-illumination window for LEO satellites is significantly extended during the summer, persisting even through the midnight hours.

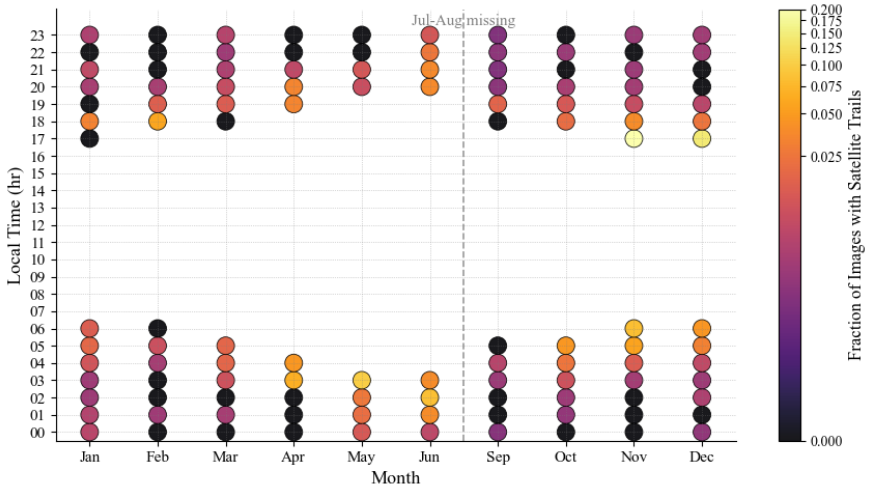

Fig. 6: Hourly fraction of images with satellite trails acquired by the 80-cm telescope in 2023.

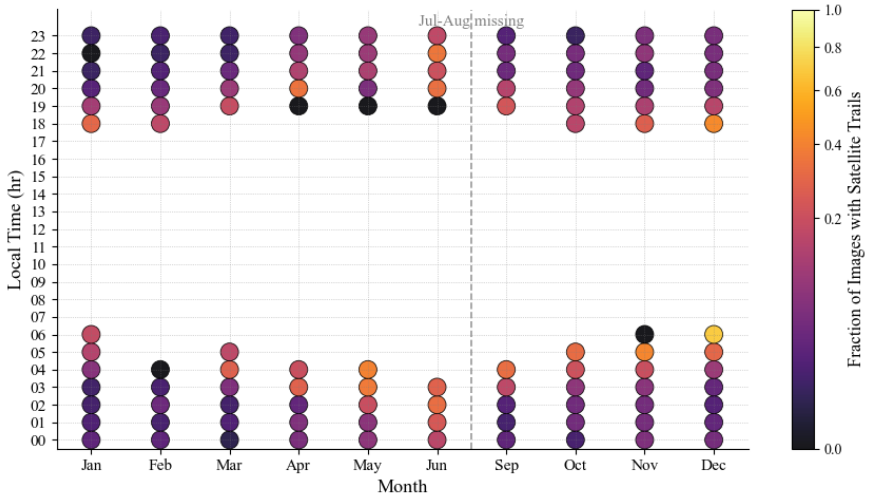

Fig. 7: Hourly fraction of images with satellite trails acquired by the MST2 in 2023.

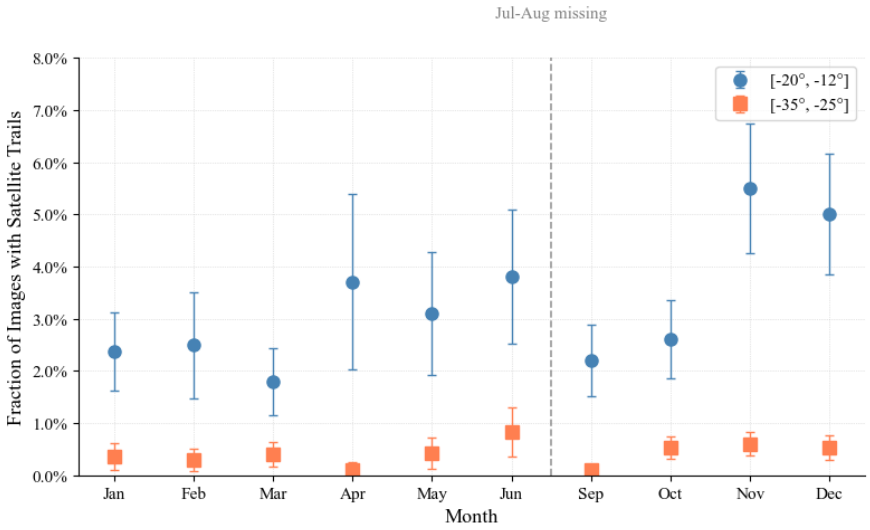

Fig. 8: Fraction of images with satellite trails acquired by the 80-cm telescope in 2023. Blue dots and orange squares represent images taken within solar elevation ranges of $-20°$ to $-12°$ and $-35°$ to $-25°$, respectively.

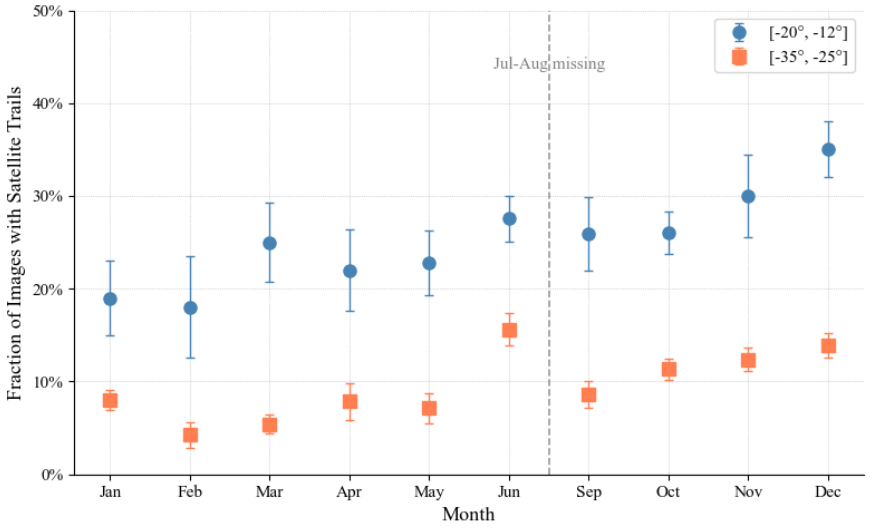

Fig. 9: Fraction of images with satellite trails acquired by the MST2 in 2023. Blue dots and orange squares represent images taken within solar elevation ranges of $-20°$ to $-12°$ and $-35°$ to $-25°$, respectively.

As expected by McDowell (2020) , twilight and summer observations are particularly vulnerable to satellite trail contamination. For deep-night observations, the fraction of contaminated images during summer is notably higher than in other months. Telescopes with wider FoVs are significantly more affected. Specifically, approximately 19% of the images acquired by the MST2 during the summer exhibit satellite trails. Furthermore, while less than 20% of twilight images were affected in January 2023, this

fraction increased to approximately 35% by December 2023. As of December 31, 2023, SpaceX has deployed more than 5,000 satellites cumulatively. While the fraction of contaminated images grows with constellation expansion, the scientific operations of both the 80-cm telescope and the MST have not yet been severely compromised. However, the number of satellites and space debris will only increase in the future, SpaceX has received FCC approval to operate up to 42,000 satellites in total (Halferty et al. 2022), and the proliferation of artificial satellites is forecast to exceed 100,000 active units in LEO before 2030 (Krantz et al. 2021). We estimate that if the full constellation of 42,000 Starlink satellites is deployed, nearly all MST images acquired during twilight will be affected. Furthermore, should the constellation scale reach 100,000 satellites, virtually all MST images acquired in summer will be affected.

4 APERTURE PHOTOMETRY

To assess the impact of satellite trails on sources, we quantify the fraction of affected sources in the detected trail-contaminated images for the 80-cm telescope and the MST2. In addition, we perform aperture photometry specifically on the MST2 images affected by satellite trails to derive source magnitudes. Subsequently, by cross-matching with the Gaia catalog, we calculate the residuals between the measured magnitudes and their Gaia counterparts: $\Delta\mathrm{mag} = \mathrm{mag}_{\mathrm{measure}} - \mathrm{mag}_{\mathrm{Gaia}}$. Finally, using $\Delta\mathrm{mag}$ of sources located near the trails as a sample, we calculate the distribution of this sample relative to $\Delta\mathrm{mag}$ of the entire source population. These data allow us to analyze the impact of satellite trails on sources at various distances and across a range of magnitudes.

4.1 Method

To analyze images containing satellite trails, we first determine the trail coordinates and widths, subsequently measuring the distance between each source and the trails. Based on the results of our subsequent analysis, we adopt a distance of 12 pixels as the threshold; sources within this distance are considered to be affected. We then quantify the fraction of affected sources in the 2023 (January–December) trail-contaminated datasets for the 80-cm telescope and the MST2 respectively.

Furthermore, we perform aperture photometry on the trail-contaminated MST2 images. To ensure the highest photometric precision across varying atmospheric conditions, we employed a set of fixed circular apertures with diameters ranging from 6 to 16 pixels ($5.2''$ to $13.8''$). For each image, the optimal aperture size was dynamically selected by minimizing the photometric uncertainty and maximizing the signal-to-noise ratio (SNR) based on the local seeing (FWHM). The majority of the samples utilized optimal apertures between 8 and 12 pixels ($6.9''$ to $10.3''$).

The resulting magnitudes are cross-matched with the Gaia catalog for photometric calibration. We subsequently calculate the residuals between our measured magnitudes and the corresponding magnitudes from the Gaia catalog: $\Delta\mathrm{mag} = \mathrm{mag}_{\mathrm{measure}} - \mathrm{mag}_{\mathrm{Gaia}}$. All sources are binned in 0.5-mag intervals based on their Gaia magnitudes. We calculate the standard deviation σ_i for each magnitude bin to derive the standardized residual σ for each source : $\sigma = (\mathrm{mag}_{\mathrm{measure}} - \mathrm{mag}_{\mathrm{Gaia}})/\sigma_i$. The sources are grouped separately based on their distance from the satellite trail (in 0.5-pixel steps) and their magnitude (in 0.5-mag steps). By computing the median standardized residuals for each bin, we assess the impact of satellite trails on sources at various distances and with different magnitudes.

4.2 Results

Figure 10 shows the monthly averaged count of affected sources and their fraction per trail-contaminated image for the 80-cm telescope and the MST2 throughout 2023. The values are first calculated for each trail-contaminated image and then averaged monthly. For the 80-cm telescope, the average fraction of affected sources per trail-contaminated image is approximately 5%, with minimal monthly fluctuation. In contrast, the fraction for the MST2 Array is approximately 0.3%, also showing little variation from month to month.

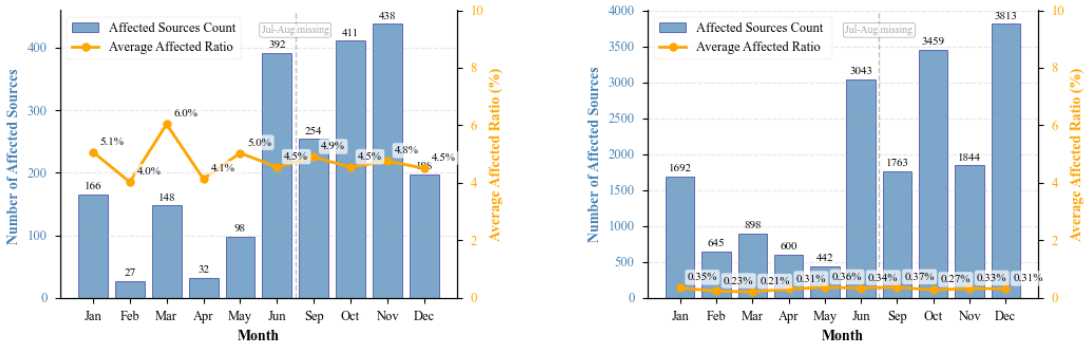

Fig. 10: Monthly average of the count of affected sources and their fraction per trail-contaminated image, shown for the 80-cm telescope (left) and the MST2 (right), from January – December 2023. Blue bars indicate the counts, and the orange line represents the fraction.

Subsequently, by incorporating the monthly fraction of images containing satellite trails, we calculate the overall fraction of sources affected with images for both the 80-cm telescope and the MST2. Figure 11 shows the fraction of affected sources in images acquired by the 80-cm telescope and the MST2 from January to December 2023. The data reveal a negligible discrepancy in the affected source fraction between the two facilities. This fraction, while currently modest, exhibits an upward trend correlated with the expanding satellite constellations. In particular, a pronounced peak emerges during summer.

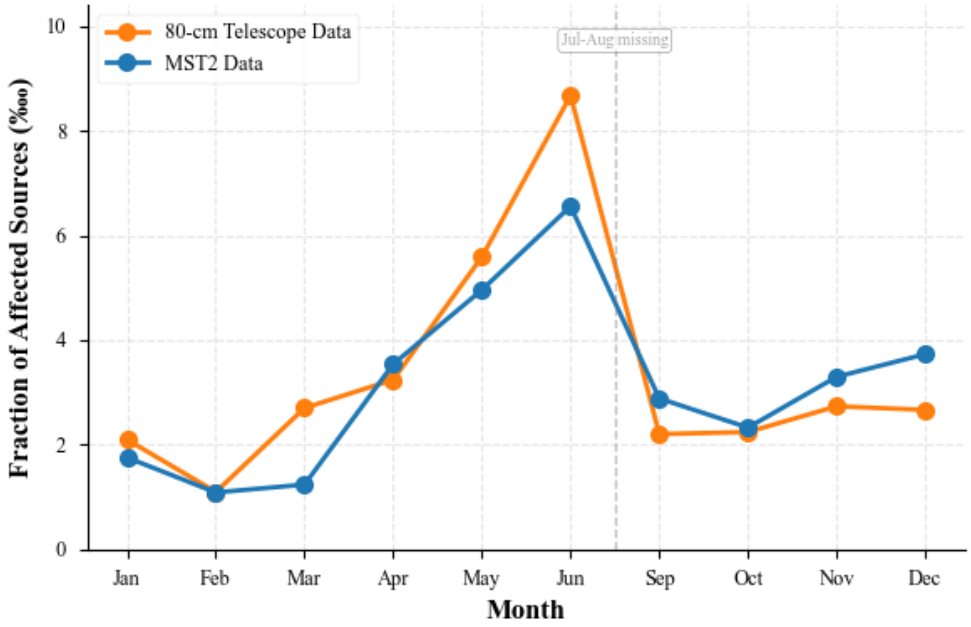

Fig. 11: Fraction of affected sources in images acquired by the 80-cm telescope and the MST2 from January to December 2023: Orange represents the 80-cm telescope, and blue represents the MST2.

To evaluate the performance of the MST2 photometric system, we analyzed the relationship between typical photometric uncertainties and Gaia G magnitudes. As illustrated in Figure 12, the median

uncertainty trend (red line) clearly reveals the evolution of photon noise as constrained by detector performance. The photometric error remains remarkably low (< 0.02 mag) for $G < 15$, rising to approximately 0.1 mag at $G \approx 18.2$. Since all satellite trail interferences are quantified using the standardized residual σ (where residuals are normalized by the intrinsic uncertainty σ_i at each magnitude level), a consistent assessment of the trail impact is maintained across varying signal-to-noise ratios.

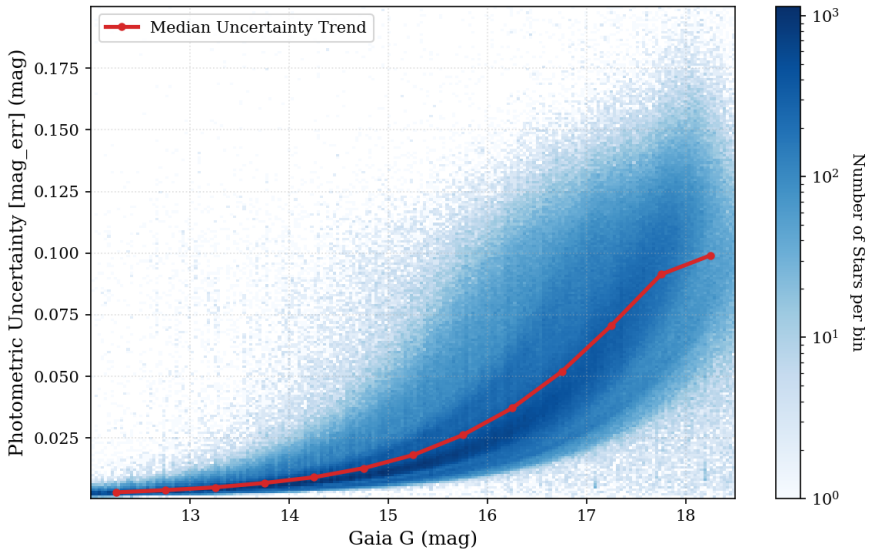

Fig. 12: 2D density distribution of photometric uncertainties (mag_err) as a function of Gaia G magnitude for the MST2 observation system.

Figure 13 separately shows the relationships between σ and the distance from the satellite trail, as well as between σ and magnitude. The left panel shows the σ of sources located within 12 pixels of the satellite trail as a function of their distance from the trail. The middle panel shows the σ of these same sources (within 12 pixels) as a function of their magnitude. For comparison, the right panel shows σ for all sources as a function of their magnitude. The red trend lines represent the median standardized residual values calculated for different distance bins and different magnitude bins, respectively.

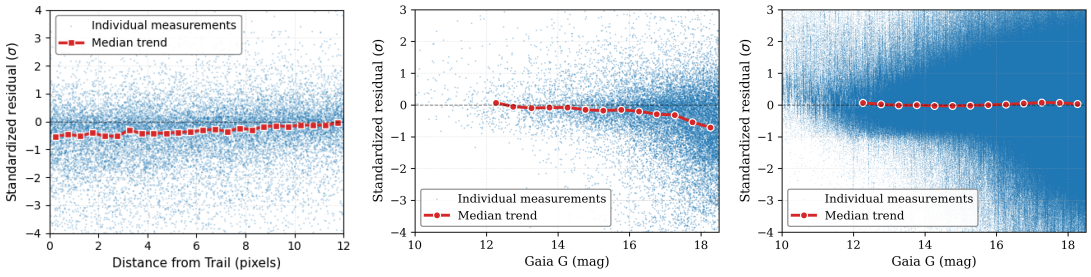

Fig. 13: Plots of the standardized residual σ versus : (left) the distance from the satellite trail for sources within 12 pixels, (center) the magnitude for sources within 12 pixels, and (right) the magnitude for all sources. The blue dots represent the measured values for each individual source, the red trend lines represent the median standardized residual values corresponding to different distance bins and different magnitude bins, respectively.

The results indicate that the impact of satellite trails intensifies with decreasing distance to the trail. Specifically, the closer a source is to the satellite trail, the more negative the median standardized residual (σ) becomes. The deviation increases from approximately 0.1σ at a distance of 11 pixels from the trail to approximately 0.5σ at a distance of 1 pixel. This trend indicates that sources appear progressively brighter in our measurements relative to the Gaia reference magnitude as they approach the trail. At a distance of 12 pixels, the median standardized residual approaches zero, suggesting that sources beyond this threshold are virtually unaffected. Regarding brightness, fainter sources experience a more pronounced impact. For sources fainter than 16 mag, the median standardized residual shifts toward negative values, the deviation increases from approximately 0.15σ at 16 mag to approximately 0.7σ at 18 mag.

To further investigate the modulation of photometric interference by atmospheric seeing, we performed a sub-group analysis based on the seeing conditions of the images: Good ($< 3.5''$), Median ($3.5''$-$4.5''$), and Poor ($> 4.5''$).

As shown in Figure 14, the median standardized residuals (σ) exhibit a pronounced dependence on seeing. In images with Poor Seeing ($> 4.5''$), the satellite trails present a broader transverse profile, which significantly increases the distance threshold at which scattered light enters the photometric aperture. Quantitatively, the median standardized residuals (σ) in the Poor Seeing group fail to return to the baseline even as the distance from the trail increases to 12 pixels. The magnitude of deviation in the Poor Seeing group is consistently and significantly larger than that in the Good Seeing group, while the latter shows much smaller deviations overall. Specifically, for the Poor Seeing group, the deviation of median standardized residuals remain greater than 0.5 σ for all sources within 8 pixels of the trail, highlighting the extended spatial impact of satellite contamination under suboptimal atmospheric conditions.

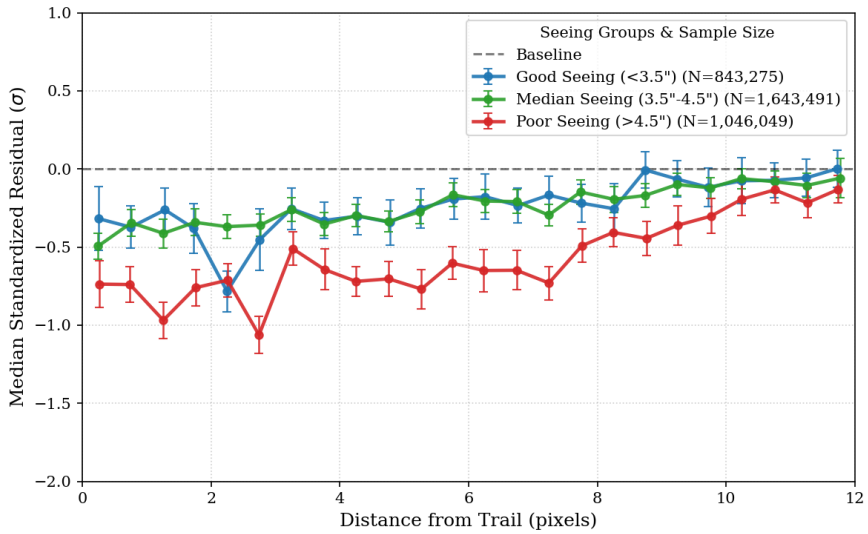

Fig. 14: Median standardized photometric residuals (σ) as a function of the distance from the satellite trail, categorized by atmospheric seeing conditions.

5 DISCUSSION

As simulation results and observational data indicate, the impact of artificial satellites on astronomical observations is escalating with the growing deployment of satellites. For wide-field telescopes such as the MST, the fraction of images containing satellite trails is significantly higher. Although the number of images containing satellite trails is gradually rising, the scientific operations of the 80-cm telescope and the MST at the Xinglong Observatory have not been severely compromised by trails at present.

The population of LEO satellites is undergoing dramatic expansion, with Starlink currently holding predominance. As the first large-scale constellation to achieve massive deployment, Starlink will not remain alone: 43 mega-constellation projects are now in active development (Zhi et al. 2024). Should SpaceX's regulatory requests for 42,000 Starlink satellites be approved, and coupled with the implementation of other proposed constellations, the proliferation of artificial satellites is forecast to escalate beyond 100,000 active units in LEO before 2030 (Krantz et al. 2021). These satellites will act as reflective surfaces for sunlight; thus, the impact on ground-based astronomical observations is projected to be significant.

Sustained astronomical monitoring programs require uninterrupted stabilized data acquisition. Satellite passages within instrument FOVs generate: stray light contamination, detector saturation, flux contamination, and changes in the image background. Such effects irreversibly compromise critical research domains like time-domain astronomy, all-sky surveys, deep-field imaging, spectroscopic observations, and surface source imaging. Facilities conducting wide-field surveys, such as the Vera C. Rubin Observatory, experience particularly severe consequences (Zhi et al. 2024).

The impacts of large constellations of LEO satellites on astronomical research and public experience are highly variable, with estimates ranging between negligible and extreme. This variation hinges on observational factors such as the specific scientific or practical objectives, the facility's etendue, the observation strategy's flexibility for satellite avoidance, and the effectiveness of trail masking or removal in data processing. Furthermore, the severity of impact is critically dependent on the characteristics of the satellites: their total population, orbital altitude, apparent brightness, orientation, and the precision of orbital ephemerides (Walker et al. 2020).

Existing research has characterized such pixel contamination rates, with the current consensus indicating minimal overall pixel loss fractions. For example, extrapolation from current observations indicates that a constellation of 42,000 Starlink satellites would contaminate approximately 0.04% of pixels in ZTF data over a year (Mróz et al. 2022). Based on our observations, we estimate the pixel loss fractions due to satellite trail contamination for the 80-cm telescope and the MST2. For the 80-cm telescope, 42,000 Starlink satellites would contaminate approximately 0.02% of pixels annually. For the MST2, the same number of satellites would affect about 0.07% of pixels per year. Nevertheless, these impacts deserve serious consideration. Primarily, their removal necessitates significant computational expenditure. More critically, such streaks can obscure transient events or Solar system objects, potentially compromising discovery opportunities.

We also discussed the impact of satellite trails on astrometric precision. Figure 15 illustrates the relationship between astrometric offset, cross-track distance, and seeing conditions. The results indicate that atmospheric seeing is the dominant factor governing astrometric uncertainty, significantly outweighing the direct contribution from the satellite trail itself. Even within the contaminated regions, the baseline seeing level (expressed as PSF dispersion) accounts for the majority of the positional uncertainty. The satellite trail acts only as a secondary factor under poor seeing conditions, inducing minor additional offsets at close range by disrupting the local symmetry of the background profile.

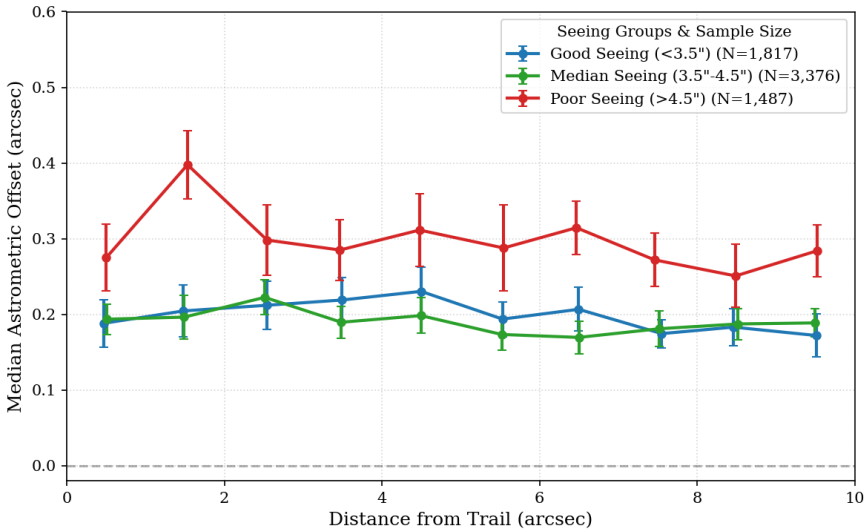

Fig. 15: Median astrometric offsets between measured centroids and Gaia reference positions relative to the distance from the satellite trail.

SpaceX's next-generation satellite platform (Gen2 v2.0) is currently in development. The precursor to this generation, designated as the V2 Mini, has a surface area more than four times as great as the Gen 1 satellites (Mallama et al. 2023a). Given the established correlation between spacecraft surface area and optical brightness, astronomers have voiced significant concern about the brightness of Starlink Gen2 satellites. To address the increased size of its satellites, SpaceX has employed a comprehensive brightness reduction strategy. The most recent observations indicate that V2 Mini satellites are actually fainter than the Gen 1 spacecraft (Mallama et al. 2023a). The company's brightness reduction strategies will face increased challenges with the deployment of future full-scale satellites (Mallama et al. 2023b).

6 CONCLUSIONS

Based on simulation and observational data, it is evident that the proliferating number of artificial satellites is increasing the impact on observations with the 80-cm telescope and the MST at the Xinglong Observatory. This interference is more pronounced during twilight and summer. The duration of satellite visibility is markedly greater in summer, leading to all night visibility, while in winter, visibility is confined to twilight. Particularly for wide-field telescopes like the MST. For the MST, the fraction of images containing satellite trails increased from 5% in January 2023 to 12% in December 2023, with a peak of 19% recorded during the summer. Furthermore, while less than 20% of twilight images were affected in January 2023, this fraction increased to approximately 35% by December 2023. For the 80-cm telescope, the fraction of images containing satellite trails increased from an average of 0.34% in 2019 to 0.7% in 2023; the impact is particularly severe during twilight. Although the number of affected images is rising with increasing satellite deployments, the scientific operations have not yet been seriously compromised. However, as the population of satellites and space debris continues to grow, future interference will escalate. We estimate that if the full constellation of 42,000 Starlink satellites is deployed, nearly all MST images acquired during twilight will be affected. Should the constellation scale reach 100,000 satellites, virtually all MST images acquired in summer will be affected. The fraction of sources affected by satellite trails remains modest for both facilities. A clear peak in this fraction is observed during the summer.

Photometric analysis demonstrates that sources in closer proximity to satellite trails and those with fainter magnitudes experience a greater impact. Specifically, at a distance of 11 pixels, the median stan-

dardized residual deviates by approximately 0.1σ; this increases to approximately 0.5σ at 1 pixel. The median standardized residual approaches zero at 12 pixels, indicating that sources beyond this threshold are virtually unaffected. Regarding brightness, the median standardized residual progressively shifts toward negative values for sources fainter than 16 mag, the deviation grows from approximately 0.15σ at 16 mag to approximately 0.7σ at 18 mag. Furthermore, comparative analysis across different seeing conditions shows that the deviation of median standardized residuals (σ) is significantly greater under poor seeing than under good seeing conditions. Specifically, for the Poor Seeing group, the deviation of median standardized residuals remain greater than 0.5 σ for all sources within 8 pixels of the trail; notably, the median standardized residuals in this group fail to return to the baseline even as the distance from the trail center increases to 12 pixels.

Future work will extend this analysis to examine satellite interference with SiTian (Liu et al. 2021) observations. As satellite populations continue to expand, it is imperative for the astronomical community to develop advanced techniques to identify, model, subtract, and mask affected pixels. Concurrently, we call for stringent regulatory frameworks at the legislative and policy levels to preserve Dark and Quiet Skies, coupled with global scientific outreach to enhance global awareness of Earth and sky protection.

Acknowledgements We acknowledge the support of the staff at the Xinglong Observatory. This work is supported by the Strategic Priority Research Program of the Chinese Academy of Sciences, Grant No. XDB0550100. Data resources are supported by China National Astronomical Data Center (NADC).

The SiTian project is a next-generation, large-scale time-domain survey designed to build an array of over 60 optical telescopes, primarily located at observatory sites in China. This array will enable single-exposure observations of the entire northern hemisphere night sky with a cadence of only 30-minute, capturing true color (gri) time-series data down to about 21 mag. This project is proposed and led by the National Astronomical Observatories, Chinese Academy of Sciences (NAOC). As the pathfinder for the SiTian project, the Mini-SiTian project utilizes an array of three 30 cm telescopes to simulate a single node of the full SiTian array. The Mini-SiTian has begun its survey since November 2022. The SiTian and Mini-SiTian have been supported from the Strategic Pioneer Program of the Astronomy Large-Scale Scientific Facility, Chinese Academy of Sciences and the Science and Education Integration Funding of University of Chinese Academy of Sciences.

References

Barentine, J. C., Venkatesan, A., Heim, J., et al. 2023, Nature Astronomy, 7, 252 1
Bassa, C., Hainaut, O., & Galadí-Enríquez, D. 2022, Astronomy & Astrophysics, 657, A75 2
Cui, Z., & Xu, Y. 2022, Astronomy and Computing, 41, 100652 3, 4
Fan, Z., Wang, H., Jiang, X., et al. 2016, Publications of the Astronomical Society of the Pacific, 128 4
Gallozzi, S., Paris, D., Scardia, M., & Dubois, D. 2020, arXiv preprint arXiv:2003.05472 2
Halferty, G., Reddy, V., Campbell, T., Battle, A., & Furfaro, R. 2022, Monthly Notices of the Royal Astronomical Society, 516, 1502 2, 3, 11
He, M., Wu, H., Ge, L., et al. 2025, Research in Astronomy and Astrophysics, 25, 044005 6
Horiuchi, T., Hanayama, H., & Ohishi, M. 2020, The Astrophysical Journal, 905, 3 3
Huang, Y., Liu, J., Wu, H., et al. 2025, Research in Astronomy and Astrophysics, 25, 044001 6
Krantz, H., Pearce, E. C., & Block, A. 2021, arXiv preprint arXiv:2110.10578 2, 11, 15
Kruk, S., García-Martín, P., Popescu, M., et al. 2023, Nature Astronomy, 7, 262 2
Lawler, S. M., Boley, A. C., & Rein, H. 2021, The Astronomical Journal, 163, 21 2
Liu, J., Soria, R., Wu, X.-F., Wu, H., & Shang, Z. 2021, Anais da Academia Brasileira de Ciências, 93, e20200628 6, 17
Mallama, A., Cole, R. E., Harrington, S., et al. 2023a, arXiv preprint arXiv:2306.06657 16
Mallama, A., Hornig, A., Cole, R. E., et al. 2023b, arXiv preprint arXiv:2309.14152 3, 16
McDowell, J. C. 2020, The Astrophysical Journal Letters, 892, L36 2, 10
Mróz, P., Otarola, A., Prince, T. A., et al. 2022, The Astrophysical Journal, 924 2, 15
Muirhead, I. J., Crisp, N. H., McGrath, C. N., & Roberts, P. C. 2025, The Astronomical Journal, 170, 215 2

Rosenfield, P., Fay, J., Gilchrist, R. K., et al. 2018, The Astrophysical Journal Supplement Series, 236, 22 3
Stoppa, F., Groot, P., Stuik, R., et al. 2024, Astronomy & Astrophysics, 692, A199 7
Tregloan-Reed, J., Otarola, A., Ortiz, E., et al. 2020, Astronomy & Astrophysics, 637, L1 3
Tyson, J. A., Ivezić, Ž., Bradshaw, A., et al. 2020, The Astronomical Journal, 160, 226 2
Walker, C., Hall, J., Allen, L., et al. 2020, Bulletin of the American Astronomical Society, 52 2, 15
Xu, Y., Cui, C., Fan, D., et al. 2020, Astronomy and Computing, 31, 100380 3
Zhang, Y., Du, L., Hu, Y., et al. 2025, Research in Astronomy and Astrophysics, 25, 044003 6
Zhi, H., Jiang, X., & Wang, J. 2024, Monthly Notices of the Royal Astronomical Society, 530, 5006 2, 15